# Structured clustering of the glycosphingolipid GM1 is required for membrane curvature induced by cholera toxin

Abir Maarouf Kabbani[1], Krishnan Raghunathan[2], Wayne I. Lencer[3], Anne K. Kenworthy[4, 5], Christopher V. Kelly[1, *]

[1] Department of Physics and Astronomy, Wayne State University, Detroit, MI USA
[2] Department of Pediatrics Infectious Disease, University of Pittsburgh School of Medicine, Pittsburgh, PA USA
[3] Division of Gastroenterology, Boston Children's Hospital, Boston, MA USA; Department of Pediatrics, Harvard Medical School, Boston, MA USA; Harvard Digestive Diseases Center, Boston, MA USA
[4] Department of Molecular Physiology and Biophysics, Vanderbilt University School of Medicine, Nashville, TN USA
[5] Present address: Center for Membrane and Cell Physiology, University of Virginia School of Medicine, Charlottesville, VA USA
*Corresponding Author. Email: cvkelly@wayne.edu; Phone: (313) 577-8473.

**Keywords**

gangliosides, toxins, binding stoichiometry, curvature generation, super-resolution, model membranes, clathrin-independent endocytosis

**ORCIDs**

Abir Maarouf Kabbani: 0000-0001-5953-1672
Krishnan Raghunathan: 0000-0003-2228-6313
Wayne I. Lencer: 0000-0001-7346-2730
Anne K. Kenworthy: 0000-0001-6567-9059
Christopher V. Kelly: 0000-0003-0886-8691

**Author Contributions**

A.M.K., K.R., W.I.L., A.K.K., and C.V.K. designed the research. A.M.K. performed the imaging. A.M.K. and C.V.K. performed the data analysis. A.M.K., K.R., W.I.L., A.K.K., and C.V.K. wrote the paper.

This PDF file includes the Abstract, Introduction, Results, Discussion, Methods, Figures 1-7, and Supplemental Figures S1-S8

## SIGNIFICANCE STATEMENT

Membrane binding toxins demonstrate both a public health challenge and a bioengineering opportunity due to their efficient internalization into cells. These toxins multivalently bind to naturally occurring lipid receptors at the plasma membrane and initiate endocytosis. This manuscript reports the importance of structured lipid-receptor clustering for the induction of membrane bending. We also observed that the magnitude of membrane curvature to be correlated to the stoichiometry of toxin-bound receptors. The initiation of curvature by these prototypical clathrin-independent cargoes provides mechanistic insight into the early steps in endocytosis.


## ABSTRACT

$AB_5$ bacterial toxins and polyomaviruses induce membrane curvature as a mechanism to facilitate their entry into host cells. How membrane bending is accomplished is not yet fully understood but has been linked to the simultaneous binding of the pentameric B-subunit to multiple copies of their glycosphingolipid receptors. Here, we probe the toxin membrane binding and internalization mechanisms by using a combination of super-resolution and polarized localization microscopy. We show that cholera toxin subunit B (CTxB) can induce membrane curvature only when bound to multiple copies of its glycosphingolipid receptor, GM1, and the ceramide structure of GM1 is likely not a determinant of this activity as assessed in model membranes. A mutant CTxB capable of binding only a single GM1 fails to generate curvature either in model membranes or in cells and clustering the mutant CTxB-single-GM1 complexes by antibody cross-linking does not rescue the membrane curvature phenotype. We conclude both the multiplicity and specific geometry of GM1 binding sites are necessary for the induction of membrane curvature. We expect this to be a general rule of membrane behavior for all $AB_5$-subunit toxins and polyomaviruses that bind glycosphingolipids to invade host cells.

## INTRODUCTION

Cholera toxin (CTx) causes the massive and often deadly secretory diarrhea following enteric infection with the bacteria *Vibrio cholerae.* 2.9 million infections and 95,000 deaths are attributed to cholera annually (1). CTx typifies the $AB_5$ family of bacterial toxins that includes the heat-labile *E. coli*, Shiga, tetanus, and pertussis toxins. The B-subunits of these toxins multivalently bind and cross-link naturally occurring plasma membrane glycosphingolipids to induce cellular internalization and guide intracellular trafficking (2). In the case of CTx, the B-subunit (CTxB) binds the glycosphingolipid GM1 to engage endogenous mechanisms of endocytic uptake and retrograde trafficking from the plasma membrane into the endoplasmic reticulum (ER). Once in the ER, the enzymatically active A-subunit co-opts the machinery for ER-associated degradation to retro-translocate into the cytosol and induce disease (3). With the exception of pertussis toxin, the B-subunits of these toxins assemble into stable and perfectly symmetrical homopentamers that can bind five or more glycosphingolipids at once and localize the toxin within plasma membrane nanodomains enriched in cholesterol (4, 5). But, how these evolutionarily conserved and highly-potent B-subunits work to enable invasion of the host cell remains incompletely understood.

Here, we test the idea that CTxB requires defined stoichiometry of binding to create *de-novo* highly-curved membranes (6–11) and to sort the toxin into such highly-curved membrane structures (11–13). Because CTxB internalization *in vivo* does not exclusively rely on either clathrin- or caveolin-dependent processes (14–21), it is feasible that an inherent membrane bending capability of CTxB may drive cellular uptake (10, 22). We examine the mechanisms by which CTxB induces membrane curvature using polarized localization microscopy (PLM). PLM provides super-resolution information on membrane orientation and detects membrane curvature with order-of-magnitude greater sensitivity than comparable optical methods (23). Curvature induction was measured in model membranes and plasma membranes of intact live-cells to test the influence of the multivalent binding of CTxB and the molecular shape and lipid phase preference of GM1. We found that membrane bending in model membranes caused by CTxB can be explained by the stoichiometry of binding at least two GM1 molecules per CTxB, and no contribution was observed from the ceramide tail structure of the GM1 or membrane cholesterol content. The need for multivalent binding to GM1 was further supported by super-resolution imaging of live cells exposed to pentavalent wild type (wt) or a monovalent mutant CTxB (mCTxB) capable of binding only a single GM1.

## RESULTS

### Stoichiometry of GM1 binding to CTxB dictates membrane curvature induction

$AB_5$ toxins such as CTx, STx, and SV40 virus are known to induce membrane curvature, likely through binding to multiple copies of their glycolipid receptors (10, 20, 22). We tested this hypothesis using CTxB that contains 5 potential binding sites for its receptor GM1 as a model system. To detect membrane curvature, we used a nanoscale membrane budding assay based on PLM (23). Using this assay, we previously showed the addition of fluorescently labeled CTxB to supported bilayers composed of POPC, DiI, and GM1 induced the growth of membrane buds with a radius of < 50 nm that subsequently grow to form tubules with a radius of > 200 nm. These membrane bending events were driven by the accumulation of CTxB at the base of the tubule, reflecting the preference of the toxin for negative Gaussian membrane curvature vs. planar or positive-curvature regions.

We first tested the effect of receptor clustering by altering the average number of GM1s bound per toxin. This was accomplished by either varying the concentration of CTxB while holding

the levels of GM1 in the membrane constant at 0.3 mol% (Fig. 1) or varying the concentration of GM1 while holding the CTxB concentration constant at 0.25 µg/mL (Fig. 2). Membrane curvature and CTxB localization were then determined independently via p-polarized localization microscopy (pPLM) and direct stochastic optical reconstruction microscopy (dSTORM), respectively (23, 24).

Reconstructed images in the two channels revealed that regions of membrane curvature were enriched in CTxB. Puncta of DiI localizations via pPLM indicated membrane buds and regions of the sample in which the membrane was perpendicular to the microscope coverslip (23). Interestingly, altering the GM1:CTxB ratio altered the radii of the membrane buds. Decreasing the GM1:CTxB ratio by increasing the concentration of CTxB from 0.01 to 0.25 µg/mL, also decreased the average bud size from a maximum value of 285 ± 66 to 53 ± 20 nm as detected by dSTORM and 116 ± 68 to 49 ± 14 nm as reported by pPLM (Fig. 1M). A similar result was observed when the GM1:CTxB ratio was varied by changing GM1 concentrations. In this case, the bud size increased with increasing concentrations of GM1. Measured values at 0.3 and 1 mol% were 50 ± 14 and 132 ± 70 nm via dSTORM and 53 ± 20 and 119 ± 50 nm via pPLM, respectively (Fig. 2J). No membrane bending was detected at the lowest GM1-to-CTxB ratios examined, including either a high concentration of CTxB (0.5 µg/mL) or a low concentration of GM1 (0.1 mol%). These findings reveal the GM1:CTxB ratio is an important factor underlying the induction of membrane curvature, with high ratios giving rise to the formation of large buds and low ratios entirely failing to initiate membrane bending. Based on our results, we hypothesized that at low GM1:CTxB ratio, the predominant stoichiometry of membrane-bound CTxB is that of a single GM1 receptor bound to each CTxB, which does not induce membrane buds.

**Monovalent CTxB does not induce membrane budding**

To test this hypothesis alternately, we determined the capacity of a monovalent variant of CTxB (mCTxB) to induce membrane curvature. Each mCTxB contains one native GM1-binding subunit and four subunits with G33D mutations that disrupt GM1 binding; each mCTxB can bind precisely one GM1 (25). We examined the ability of 0.1 or 0.5 µg/mL of mCTxB to induce curvature in membranes containing 0.3 mol% GM1. These concentrations of mCTxB were chosen to match the protein concentration and active GM1 binding site concentration, respectively, of the 0.1 µg/mL wtCTxB condition that consistently induced membrane bending (Fig. 1B). In contrast to the behavior of wtCTxB that contained 5 GM1 binding sites, no change in membrane topography was detected upon the addition of mCTxB to membranes at either concentration in model membranes (Fig. 3 and S1). To confirm the effect of valency on CTxB-induced curvature, we determined if mCTxB is capable of inducing curvature in intact giant unilamellar vesicles (GUVs). CTxB induced membrane invaginations on GUVs as expected (10), whereas mCTxB caused no apparent change to the membrane shape (Fig. S1). Thus, the binding of CTxB to a single GM1 is not sufficient to bend membranes.

**Spatial organization of GM1 binding is necessary for inducing membrane curvature**

We next tested the hypothesis that the spatial organization of binding sites on CTxB critically underlies the generation of membrane curvature. To test this idea, we asked if the clustering of monovalent CTxB by antibody cross-linking could override the requirement for multivalent binding by CTxB. For these experiments, membrane-bound mCTxB was cross-linked with varying amounts of anti-CTxB antibodies. The highest antibody concentrations used (1:100 dilution) induced clustering of mCTxB into punctate structures (Fig. 3 and S2) and significantly

slowed the diffusion of mCTxB (Fig. S3). However, no membrane bending was observed by pPLM at any anti-CTxB concentration examined.

We also tested if a general protein-induced clustering of lipids is sufficient to induce curvature. We labeled membranes containing varying concentrations of DPPE-biotin and crosslinked the lipids using streptavidin (Fig. S4). The tetravalent binding of streptavidin to DPPE-biotin yielded no apparent variations in the membrane topography as assessed with pPLM at any of the streptavidin or DPPE-biotin concentrations tested, consistent with previous reports (26). Taken together, these findings support the hypothesis that the spatial organization of GM1 binding sites in CTxB is important for the curvature generation process. The curvature generation cannot be explained as a consequence of the protein-induced clustering of lipids in the absence of the geometry induced by the pentameric B-subunit.

**Single-particle tracking reveals complexes with high GM1-to-CTxB ratios diffuse extremely slowly**

We used the diffusional behavior of CTxB-GM1 complexes to gain further insights into the stoichiometry of GM1 bound to CTxB in the membrane buds. To probe the dynamics of CTxB-GM1 complexes, the single-molecule blinking data used in the reconstruction of super-resolution images for wtCTxB and mCTxB were analyzed using high-throughput single-particle tracking. To eliminate the possibility of topographical effects slowing diffusion, we excluded any single-particle trajectories that were coincident with punctate localizations in pPLM. As a control, an identical analysis was performed for DiI, and minimal effects of CTxB binding were observed on DiI diffusion. Under all experimental conditions tested, DiI exhibited diffusion consistent with a single population diffusion coefficient ($D$) of 0.46 ± 0.2 μm$^2$/sec.

mCTxB, like DiI, demonstrated a single population of Brownian diffusers with a characteristic $D$ of 0.74 ± 0.54 μm$^2$/s. In contrast, wtCTxB displayed heterogeneous, multi-population distributions of diffusion coefficients. Greater GM1 availability increased the abundance, but not the speed, of the slower moving populations of wtCTxB (Fig. 4 and S5).

To discern the underlying populations, the experimentally acquired distributions of $D$ were fit to a probability distribution ($P$) composed from a sum of subpopulations of diffusers (Eq. 1) with each subpopulation contributing a log-normal distribution of $D$ (Eq. 2).

$$P_{Full}(D) = \sum_{i=1}^{5} A_i P_{sub}(D, \mu_i) \tag{1}$$

$$P_{sub}(D, \mu_i) = \frac{1}{D\sigma_i\sqrt{(2\pi)}} e^{\left(-\frac{(\ln D - \mu_i)^2}{2\sigma^2}\right)} \tag{2}$$

The width of the log-normal distribution ($\sigma$) was assumed to be as theoretically expected from the distribution of trajectory lengths analyzed and constant for all subpopulations (27); $\sigma$ = 0.78. The mean diffusion coefficient for each subpopulation ($D_i$) is equal to $\exp(\mu_i+\sigma^2/2)$.

Three subpopulations were sufficient to fit all our data of CTxB diffusing on model membranes. $D_i$ values of $D_1$ = 0.75, $D_2$ = 0.26, and $D_3$ = 0.022 μm$^2$/s were identified by fitting the eight experimentally acquired data sets simultaneously (Fig. S5). We interpret $D_i$ as the mean diffusion coefficient for CTxB with $i$ GM1 per CTxB, i.e., $D_1$, $D_2$, and $D_3$, correspond to the diffusion rates of CTxB bound to 1, 2, and 3 GM1, respectively. The subpopulations of 4 or 5 GM1-to-CTxB were scarce and were not apparent in our super-resolution observation (*i.e.*, $A_4 = A_5 = 0$). The absence of these populations is in line with the previous MD observations that these higher-order bindings are indeed rare (28). The sum of the three fit $A_i$ values were normalized to represent the

relative fraction of CTxB with 1, 2, or 3 GM1 per CTxB in each experiment (Fig. 4B, D). As expected, the experiments with mCTxB, concentrated CTxB, or dilute GM1 each yielded $A_1$ close to unity, confirming one GM1 per CTxB. In contrast, with decreasing CTxB concentration or increasing GM1 concentration, the subpopulations that represented more GM1-per-CTxB became prevalent.

In addition to confirming the presence of multiple stoichiometries of CTxB-GM1 complexes, the results of these experiments show the diffusion coefficients do not scale linearly with the number of bound GM1 molecules. The dramatic slowing of CTxB diffusion with increasing GM1:CTxB suggests that CTxB either progressively penetrates the membrane or induces local membrane deformations that slow their diffusion. Taking these results together with the PLM results, we conclude that the binding of CTxB to just two GM1 was sufficient to induce membrane curvature. Furthermore, increasing the binding stoichiometry increased the radii of the buds.

**Impact of ceramide structure and cholesterol on curvature induction by CTxB**

The ceramide structure of GM1 functions as a key regulator of intracellular trafficking of both GM1 itself as well as CTxB-GM1 complexes (29), suggesting it plays an essential function in sorting as the toxin moves from one intracellular compartment to another. Furthermore, GM1 structure has been directly linked to the ability of SV40 to induce membrane curvature (10). We thus tested the hypothesis that the fatty acyl chains of the ceramide domain of GM1 are important for toxin-induced membrane curvature. Three custom gangliosides were used to address this question, recognizing that longer and saturated acyl tails are more correlated with ordered lipid phases (Fig. S6). In our model systems, membrane bending was detected at similar levels for $GM1_{16:1}$, $GM1_{18:1}$, or $GM1_{18:0}$ upon the addition of CTxB, and there was no systematic change in the radii of the buds correlated with the expected lipid phase preferences of the tails (Fig. 5M).

Cholesterol levels strongly regulate endocytosis of CTxB (30). We thus wondered if cholesterol levels might control the ability of CTxB to induce membrane curvature. To test this, we added 30 mol% cholesterol to the supported bilayers. Just as in the absence of cholesterol, in the presence of cholesterol, higher CTxB concentrations resulted in less membrane bending (Fig. S7). The bud radii obtained in samples with and without cholesterol were 50 ± 14 and 57 ± 15 nm via dSTORM and 54 ± 14 and 58 ± 15 nm via pPLM, respectively, when 0.1 µg/mL CTxB and 0.3 mol% $GM1_{Ovine}$ were used (Fig. 5M). Thus, neither the ceramide structure nor cholesterol inclusion impacted the capacity of CTxB to induce curvature in artificial membranes under the conditions of our experiments.

Diffusion coefficient of CTxB when bound to $GM1_{16:1}$, $GM1_{18:1}$, $GM1_{18:0}$, $GM1_{Ovine}$, or in the presence of cholesterol was 0.29 ± 0.27, 0.25 ± 0.23, 0.22 ± 0.21, 0.21 ± 0.17, and 0.081 ± 0.08 $\mu m^2$/sec, respectively. The trend observed in the distribution of diffusion coefficients is consistent with slower diffusion for lipidations and membranes of greater acyl tail order (Fig. 5N).

**GM1 binding stoichiometry affects membrane bending in cells**

Finally, we tested if the requirement for multivalent binding by CTxB to induce curvature is also conserved in cellular membranes. We assayed for curvature induction upon CTxB binding in COS-7 cells using polarized localization microscopy (14, 31). 0.1 µg/mL of CTxB or mCTxB was applied to live COS-7 cells stained with DiI (Fig. 6). Cells labeled with CTxB displayed punctate accumulations of DiI and CTxB, with a mean bud radius of 220 ± 160 nm and 260 ± 150 nm as detected by pPLM and dSTORM, respectively. There were no apparent puncta in cells labeled with both DiI and mCTxB, indicating that multivalent GM1 binding was also required to generate membrane curvature in cells.

To quantify this difference, we performed spatial cross-correlation analysis and assessed the characteristic abundance, size, and colocalization of the punctate structures (Fig. 6G). Significant cross-correlation between pPLM and CTxB was observed, demonstrating that the protein localization was spatially coincident with curved membranes with a characteristic radius of 85 to 105 nm. In contrast, pPLM and mCTxB showed negligible cross-correlation. The amplitude of spatial autocorrelations of CTxB and pPLM after CTxB addition ($pPLM_{CTxB}$) were 14-fold higher than those for mCTxB and pPLM after mCTxB addition ($pPLM_{mCTxB}$). We conclude there is a substantial increase in nanoscopic membrane bending events when CTxB, but not mCTxB, is added to cells (Fig. 6G).

To confirm the differential membrane binding induced by CTxB and mCTxB binding to cells, single-molecule diffusion coefficients were again examined (Fig. S8). On live cells, CTxB and mCTxB displayed $D$ of 0.33 ± 0.40 and 0.17 ± 0.20 $\mu m^2/s$, respectively.

## DISCUSSION

The clustering of lipids by AB5 toxins and SV40 virus is thought to induce compression of the lipids as a means of bending membranes (10, 22, 32) via a process linked to the geometry of receptor binding sites (9, 33). However, much of this process warrants further characterization, including the role of the clustering and leaflet asymmetry in the generation of curvature (34). In this study, we investigated the factors that drive membrane bending by CTxB, a prototypical cargo for clathrin-independent endocytosis, using super-resolution polarized localization microscopy.

Our data support the hypothesis that toxin-induced glycolipid crosslinking induces membrane curvature in both model membranes and cellular environments. We also show that the multivalent binding of GM1 by CTxB is necessary for the membrane curvature and experimentally demonstrate the importance of GM1-to-CTxB stoichiometry in the membrane bending capability of CTxB. Importantly, lipid scaffolding on its own is not sufficient to induce membrane bending. Thus, the mechanism by which CTxB induces curvature likely does not arise from protein crowding effects (35) but does arise as a consequence of the spatial organization of glycolipids induced by multivalent binding to pentavalent CTxB.

We also determined the likely stoichiometry of GM1 binding to CTxB by fitting the histogram of the diffusion rate to the expected log-normal Gaussian (Eq. 2). While mCTxB engineered with a single binding site had only a single population of diffusers, wtCTxB had multiple species. The distribution of $D$ of wtCTxB was best fit to three populations representing CTxB bound to 1, 2, or 3 GM1. These are consistent with simulations that show that only three of the five putative binding sites of CTxB are typically bound to GM1 (36). The diffusion rates observed here are consistent with the variety of previously published average diffusion rates (11, 14, 37–43). Furthermore, we observe a non-linear effect on the diffusion coefficient on increasing the stoichiometry of binding of GM1 to CTxB. Our results also show that CTxB bound to 3 GM1 is almost thirty times slower than CTxB bound to 1 GM1. This slowdown is greater than what is predicted by the free draining limit (44, 45), which would predict that increased GM1 per CTxB is correlated with membrane perturbations in addition to GM1 cross-linking (46). Our data also shows that the relative distribution of these populations varies with the relative concentration of GM1 and wtCTxB. Increasing the stoichiometry of attachment increases the engagement of CTxB to the bilayer. Decreasing CTxB concentration or increasing GM1 concentration results in higher subpopulations that have more GM1-per-CTxB.

Based on these findings, we propose a model for how the stoichiometry of GM1 binding to cholera toxin can be mechanistically linked to curvature generation (Fig. 7). With zero GM1

bound per CTxB, the CTxB is not membrane-bound, and there is no curvature generation. With one GM1 bound, the CTxB is attached to the membrane, but there is still no curvature generation (Fig. 7A). This single-bound-GM1 conformation likely includes the CTxB sitting tilted on the membrane to juxtapose the single GM1 binding pocket in close proximity to the membrane with minimal membrane shape dependence, as observed previously in computational models (9, 36, 47, 48). With two GM1s bound, however, CTxB has a strong preference for negative curvature along one dimension and a weak preference for negative membrane curvature along the perpendicular dimension (Fig. 7B). Further increasing the stoichiometry of CTxB binding to GM1 increasingly perturbs the membrane, giving rise to an enhanced preference towards negative curvature; this is detected in our experiments as tubules with larger radii.

Our results provide insights into the steps in the endocytosis and trafficking of cholera toxin that rely on the ability of the toxin to induce curvature. CTxB can be internalized through different endocytic pathways (15, 19, 49), including via tubular clathrin-independent carriers generated in response to toxin binding (10, 22, 50–52). Our results support the notion that wild type toxin is inherently capable of initiating membrane bending events and that curvature induction requires the toxin to bind multiple GM1. However, monovalent variants of CTxB are efficiently sorted into surface-attached endocytic tubules (50). Furthermore, “chimeric” toxins with differential number of GM1 binding sites can undergo endocytosis albeit less efficiently compared to wild type cholera toxin (53), and binding of CTxB to a single GM1 is sufficient to complete the intoxification pathway (25). Given that the ability of CTxB to induce curvature is dependent on multivalent binding to GM1, these findings suggest the CTxB-induced curvature is not required for sorting of toxin into nascent endocytic structures, entry of the toxin into cells by endocytosis, or directing its intracellular transport into pathways that leads to toxicity. However, the conditions in which CTxB induces curvature to enhance the efficacy of the toxin, perhaps due to the recruitment of ancillary host proteins that facilitate endocytosis (51, 52) or the increased affinity of the CTB-GM1 complex for curved membrane structures (*i.e.*, sorting tubules or endocytic pits).

It is well known that the ceramide structure is important for intracellular lipid sorting pathways and influences the ability of AB5 toxins to bend membranes. Unsaturated GM1 is a better receptor for retrograde trafficking of cholera toxin to the endoplasmic reticulum than saturated GM1 (29). In the case of another AB5 toxin, Shiga toxin, the side chains of its glycolipid receptor are required to be unsaturated for tubulation in artificial vesicles (22). Furthermore, long-chain but not short-chain GM1 is essential for SV40 to generate membrane invaginations (10). Motivated by these findings, we tested the hypothesis that the ceramide structure of GM1 would be relevant to the initial membrane bending process using both synthesized and naturally occurring GM1 variants. Our experiments showed there was minimal change in membrane topography in model membranes containing GM1 variants. This result suggests that CTxB-induced membrane bending does not rely on the acyl chain identity of GM1, at least within the range of the ceramide structures tested in this study. Our experiments were performed only in artificial membranes, and we do not rule out the possibility that ceramide structure may impact the ability of CTxB to generate membrane curvature in the cell surface or intracellular membranes of intact cells. In phase-separated vesicles, for instance, ceramide tail structure is critical for raft partitioning of both uncrosslinked and CTxB-crosslinked GM1 (29). Thus, ceramide structure could impact the raft association of cross-linked GM1, which is credited with the membrane bending and internalization of CTxB in cells (31, 54–56). Variation in the ceramide tail structure may alter the composition and acyl-tail order of GM1-rich nanoscopic domains (37, 57, 58). Accordingly, the spontaneous recruitment of liquid-order

preferring lipids and the line tension surrounding the GM1-rich domain are likely to depend on the ceramide structure. Given the importance of ceramide structure in various physiological contexts, we hypothesize that the role of the GM1 ceramide domain is to recruit the downstream endocytic machinery, such as clathrin, caveolin, flotillin, or dynamin.

These results also have implications for the use of cholera toxin as a marker for the liquid-ordered (raft) lipid phase. CTxB is not a non-perturbing marker for ordered domains; it can induce phase separation in membranes close to a demixing point (54, 59), stabilize ordered phases (59, 60), sort to already curved membranes (6, 11, 12), and induce membrane curvature (10, 11). Our current findings reveal that any measurements of the impact of CTxB on a membrane require precise control of the CTxB and GM1 concentrations because the diffusive, sorting, and curvature-inductive properties of CTxB depend on its binding stoichiometry.

## MATERIALS AND METHODS

**Custom GM1 synthesis.** GM1 variants in the ceramide were synthesized in DMSO solvent containing 1 μmole lyso-GM1, 10 μmoles fatty acid, 10 μmoles of dicyclohexyl-carbodiimid and 10 μmoles of sulfo-N-hydroxysuccinimide for 3 hours at room temperature, as described previously (29). The DMSO was evaporated using a Speed Vac (Thermo Fisher Scientific) and purified following established methods via a silica column, preparative-TLC plates, and reversed-phase Bond-Elut cartridges (61). The products were analyzed by electrospray ionization mass spectrometry with a quadrupole orthogonal time-of-flight instrument (Q-o-TOF MS, Q-Star Pulsar *i*, Applied Biosystems, Toronto, Canada).

**SLB preparation and formation.** SLBs were made from bursting GUVs that included 1-palmitoyl-2-oleoyl-sn-glycero-3-phosphoch (POPC; Avanti Polar Lipids), 1,1'-dioctadecyl-3,3,3',3'-tetramethylindocarbocyanine perchlorate (DiI; Life Technologies, Carlsbad, CA), and GM1. Commercially available Ovine GM1 (Avanti Polar Lipids) or GM1 with custom acyl tails were used. Typically, 0.3 mol% of DiI and 0.3 mol% of GM1 were included. For streptavidin-biotin binding experiments, GM1 was replaced with DPPE-Biotin (Avanti Polar Lipids).

GUVs were prepared by electroformation, as described previously (62). Briefly, a hydration solution of 200 mM sucrose was added to the dried lipids on an ITO slide. A chamber was created with a silicone frame and a second ITO plate enclosing the lipids and sucrose solution. The two ITO plates were connected to a sine wave function generator at 2 $V_{peak\text{-}to\text{-}peak}$ and 10 Hz for 3 hr at 50 °C.

**CTxB and mCTxB.** Alexa Fluor 647-CTxB was obtained from Invitrogen. Alexa Fluor 488-mCTxB was made as described previously (25, 31). Briefly, an *E. coli* expression strain containing the plasmids encoding native CTxB-G33D (non-binding mutant) and C-terminal GS-H6-tagged wtCTxB was induced. Each subunit was secreted to the periplasm where mixed pentamers assembled. This mixture of assembled was purified from a cell extract by Talon affinity chromatography and separated into individual species by ion-exchange chromatography. Further purification was performed by cationic resin, HQ20 anion exchange column, and anion exchange prior to buffer exchange into PBS by ultrafiltration using an Amicon Ultra-4 (Millipore) 10 K cutoff centrifugal filter. Labeling was performed by reacting Alexa Fluor 488-succinimidyl ester (Invitrogen) to 300 µg mCTxB in 100 mM sodium bicarbonate buffer pH 8.3 for 1 h under stirring at room temperature and purified using provided size exclusion chromatography resin. DiI replaced DiD in the experiments on model membranes with the mCTxB-AF488 addition to decrease channel crosstalk. Model membranes were labeled by CTxB and mCTxB with a 0.5 min

of incubation, after which the unbound CTxB or mCTxB was rinsed away. The resulting membrane budding showed no change 20 min after CTxB was added; imaging was performed approximately 60 min after CTxB addition.

**Cell Labeling.** DiI-C18 (Sigma-Aldrich) was dissolved in ethanol at 1 mM. Cells were rinsed twice with HEPES-based cell imaging buffer (Sigma-Aldrich), and the 1 mM DiI-C18 stock solution was added to Cos7 cells in HEPES at 1:100 dilution for 10 sec prior to washing with excess HEPES buffer. Cells were exposed to 0.1 µg/mL CTxB-AF647 or mCTxB-AF488 for 5 min at room temperature prior to rinsing twice with HEPES imaging buffer prior. 7 individual cells were analyzed per condition.

**Anti-CTxB antibody addition.** mCTxB crosslinking was induced by the addition of anti-CTxB antibodies (Calbiochem, 227040 goat pAb). Antibodies were added to the membrane at the 90 min time point following mCTxB addition at final dilutions of 1:10,000, 1:1000, 1:500, and 1:100 and allowed to incubate for 30 min prior to imaging.

**Imaging optics.** Dual-color imaging was performed with a custom IX83 (Olympus). The excitation light polarization was controlled by a liquid crystal wave plate (LCC1111-A; Thorlabs). The excitation lasers were steered through a periscope and a 4-band notch filter (ZET405/488/561/640m; Chroma) onto the back of a 100x, 1.49 NA objective (Olympus). The emitted light passes through emission filters (BrightLine single-band bandpass filters; Semrock) within an OptoSplit with a 2.5X magnification lens (Cairn Research) before being collected by an iXon-897 Ultra EMCCD camera (Andor Technology).

Samples were exposed to high laser power (>80 mW) with $\lambda_{ex}$ = 488 nm (mCTxB-AF488), $\lambda_{ex}$ = 561 nm (DiI), or $\lambda_{ex}$ = 647 nm (CTxB-AF647 or DiD) to provide a steady rate of photo-switching by the fluorescent probes. Sample imaging was performed 90 min after CTxB addition. 40,000 frames of blinking fluorophores were acquired for each two-color channel with an 18 ms exposure time at a 50 Hz frame rate.

**Imaging buffer**. PLM and dSTORM were performed on SLBs surrounded by an oxygen-scavenging buffer (150 mM NaCl, 50 mM TRIS, 0.5 mg/mL glucose oxidase, 20 mg/mL glucose, 40 µg/mL catalase, and 1% β-mercaptoethanol at pH 8). This buffer encourages the reversible blinking of fluorophores in a low oxygen concentration. Buffer proteins were purchased from Sigma-Aldrich (St. Louis, MO), and salts were purchased from Thermo Fisher Scientific.

**Single-molecule localization.** Single-fluorophore localizations were identified by the ImageJ plugin ThunderSTORM using bilinear interpolation to achieve sub-pixel precision (63). Single-fluorophore localizations with intensities <100 photons or location uncertainty >45 nm were excluded from the analysis. Channel co-registration was performed based on maximizing the cross-correlation between the color channels. The separate channel images were overlaid via a custom-made MATLAB routine (The MathWorks, Natick, MA) by aligning the TetraSpeck nanoparticles (100 nm diameter; Life Technologies) that were visible in all channels and maximizing the cross-correlation. Localizations of the TetraSpecks were removed from the reconstructed images and all further analysis.

**Bud identification and size evaluation**. The detection of membrane buds in each color channel was performed by a custom-made MATLAB program that masks regions with a low local

density of localizations to identify regions of curvature as described previously (23). 2D Gaussian fitting for small buds (<150 nm) and 2D toroidal fitting for buds (>150 nm) that had a ring shape were performed for center estimation. The size of the bud was calculated by evaluating the mean distance of all localizations at the bud location while considering the additional localizations from the surrounding flat membrane, as done previously (23). The number of localizations expected within a radius R if no bud was present ($N_{SLB}$); $N_{SLB} = \rho\pi R^2 = N_{all} - N_{bud}$, where $\rho$ is the uniform density of localizations on a flat membrane, $N_{bud}$ is the number of extra localizations due to the presence of the bud. The mean distance of the localizations from the center of the bud expected for the flat SLB within $R$ is $2R/3$. By analyzing all collected localizations within R and subtracting the expected localizations from the flat SLB, the size of a single budding event ($r_{bud}$) was calculated according

$$r_{bud} = \sum r_i / N_{\text{bud}} - 2\pi\rho R^3 / 3N_{\text{bud}}. \quad (3)$$

**Single-particle tracking.** Single fluorophores were analyzed to reveal the diffusion rates of the lipid and toxin. Blinking fluorophores were linked based on their proximal distance in consecutive frames via u-track (64), and single trajectories that lasted ≥15 frames were further analyzed. The slope of the single-molecule MSD vs. $\Delta t$ for $\Delta t$ from 2 to 4 frames were fit to obtain the single-molecule diffusion rates according to

$$MSD(\Delta t) = 4D\Delta t(1 + B) - 2s^2. \quad (4)$$

The localization imprecision ($s$) and the motion blur coefficient ($B$) were equal to 15 nm and 1/6, respectively, for the imaging parameters used here (65).

**Image correlation analysis.** Spatial cross-correlation of two images, $I_1$ and $I_2$, were computationally calculated according to Eq. 5 and azimuthally averaged, as done previously (66).

$$C(\bar{r}) = Re\left(\frac{FFT^{-1}\left(FFT(I_1)x\ conj\left(FFT(I_2)\right)\right)}{\rho_1\rho_2 W(r)}\right). \quad (5)$$

FFT represents the fast Fourier transform, *conj* represents the complex conjugate, and *Re* represents taking only the real component. The correlations are normalized by the average localization density ($\rho$) and the azimuthally averaged autocorrelation of the region of interest ($W$). The autocorrelation of an image, $I_1$, was calculated from Eq. 5 by setting $I_2 = I_1$.

**ACKNOWLEDGMENTS**

We thank Eric Stimpson, KeVaughna Patrick, Sonali Gandhi, Meshari Al Rafidi, Xin Xin Woodward, and Stephanie Schmieder for helpful discussions. WIL and AKK provided mCTxB. WIL provided the custom GM1. AMK was funded by a Thomas C. Rumble Fellowship Award. Financial support was provided by Wayne State University laboratory start-up funds and the Richard J. Barber Interdisciplinary Research Program. KR was supported in part through by Children's Hospital of Pittsburgh of the UPMC Health System. This material is based upon work supported by the National Science Foundation under grant no. DMR-1652316 and the National Institute of General Medical Sciences of the National Institutes of Health under Award Number R01GM106720. The content is solely the responsibility of the authors and does not necessarily represent the official views of the National Institutes of Health.

## REFERENCES


1. M. Ali, A. R. Nelson, A. L. Lopez, D. A. Sack, Updated Global Burden of Cholera in Endemic Countries. *PLoS Negl. Trop. Dis.* **9**, e0003832 (2015).

2. T. Beddoe, A. W. Paton, J. Le Nours, J. Rossjohn, J. C. Paton, Structure, Biological Functions and Applications of the AB5 Toxins. *Trends Biochem. Sci.* **35**, 411–418 (2010).

3. N. L. B. Wernick, D. J.-F. Chinnapen, J. A. Cho, W. I. Lencer, Cholera Toxin: An Intracellular Journey into the Cytosol by Way of the Endoplasmic Reticulum. *Toxins* **2**, 310–325 (2010).

4. D. J.-F. Chinnapen, H. Chinnapen, D. Saslowsky, W. I. Lencer, Rafting with cholera toxin: endocytosis and trafficking from plasma membrane to ER. *FEMS Microbiol. Lett.* **266**, 129–137 (2007).

5. C. A. Day, A. K. Kenworthy, Tracking microdomain dynamics in cell membranes. *Biochim Biophys Acta-Biomembr* **1788**, 245–253 (2009).

6. A. Tian, T. Baumgart, Sorting of Lipids and Proteins in Membrane Curvature Gradients. *Biophys. J.* **96**, 2676–2688 (2009).

7. W.-T. Hsieh, *et al.*, Curvature Sorting of Peripheral Proteins on Solid-Supported Wavy Membranes. *Langmuir* **28**, 12838–12843 (2012).

8. Y. Kaizuka, J. Groves T., Bending-mediated superstructural organizations in phase-separated lipid membranes. *New J. Phys.* **12**, 095001 (2010).

9. W. Pezeshkian, L. J. Nåbo, J. H. Ipsen, Cholera toxin B subunit induces local curvature on lipid bilayers. *FEBS Open Bio* **7**, 1638–1645 (2017).

10. H. Ewers, *et al.*, GM1 structure determines SV40-induced membrane invagination and infection. *Nat. Cell Biol.* **12**, 11–18 (2010).

11. A. M. Kabbani, C. V. Kelly, Nanoscale Membrane Budding Induced by CTxB and Detected via Polarized Localization Microscopy. *Biophys. J.* **113**, 1795–1806 (2017).

12. Y.-S. Ryu, *et al.*, Reconstituting ring-rafts in bud-mimicking topography of model membranes. *Nat. Commun.* **5**, 4507 (2014).

13. Y.-S. Ryu, *et al.*, Curvature Elasticity-Driven Leaflet Asymmetry and Interleaflet Raft Coupling in Supported Membranes. *Adv. Mater. Interfaces* **5**, 1801290 (2018).

14. C. A. Day, A. K. Kenworthy, Mechanisms underlying the confined diffusion of cholera toxin B-subunit in intact cell membranes. *PloS One* **7**, e34923 (2012).

15. M. L. Torgersen, G. Skretting, B. van Deurs, K. Sandvig, Internalization of cholera toxin by different endocytic mechanisms. *J. Cell Sci.* **114**, 3737–3747 (2001).

16. R. D. Singh, *et al.*, Selective Caveolin-1–dependent Endocytosis of Glycosphingolipids. *Mol. Biol. Cell* **14**, 3254–3265 (2003).

17. G. H. Hansen, *et al.*, Cholera toxin entry into pig enterocytes occurs via a lipid raft- and clathrin-dependent mechanism. *Biochemistry* **44**, 873–882 (2005).

18. D. V. Broeck, A. R. Lagrou, M. J. De Wolf, Distinct role of clathrin-mediated endocytosis in the functional uptake of cholera toxin. *Acta Biochim. Pol.* **54**, 757–767 (2007).

19. H. Pang, P. U. Le, I. R. Nabi, Ganglioside GM1 levels are a determinant of the extent of caveolae/raft-dependent endocytosis of cholera toxin to the Golgi apparatus. *J. Cell Sci.* **117**, 1421–1430 (2004).

20. H. Ewers, A. Helenius, Lipid-Mediated Endocytosis. *Cold Spring Harb. Perspect. Biol.* **3**, a004721 (2011).

21. L. Johannes, R. G. Parton, P. Bassereau, S. Mayor, Building endocytic pits without clathrin. *Nat. Rev. Mol. Cell Biol.* **16**, 311–321 (2015).

22. W. Römer, *et al.*, Shiga toxin induces tubular membrane invaginations for its uptake into cells. *Nature* **450**, 670–675 (2007).

23. A. M. Kabbani, C. V. Kelly, The Detection of Nanoscale Membrane Bending with Polarized Localization Microscopy. *Biophys. J.* **113**, 1782–1794 (2017).

24. S. van de Linde, *et al.*, Direct stochastic optical reconstruction microscopy with standard fluorescent probes. *Nat. Protoc.* **6**, 991–1009 (2011).

25. M. G. Jobling, Z. Yang, W. R. Kam, W. I. Lencer, R. K. Holmes, A Single Native Ganglioside GM1-Binding Site Is Sufficient for Cholera Toxin To Bind to Cells and Complete the Intoxication Pathway. *mBio* **3**, e00401-12 (2012).

26. S. Manley, M. R. Horton, S. Lecszynski, A. P. Gast, Sorting of Streptavidin Protein Coats on Phase-Separating Model Membranes. *Biophys. J.* **95**, 2301–2307 (2008).

27. M. J. Saxton, Single-particle tracking: the distribution of diffusion coefficients. *Biophys. J.* **72**, 1744–1753 (1997).

28. S. Lauer, B. Goldstein, R. L. Nolan, J. P. Nolan, Analysis of cholera toxin-ganglioside interactions by flow cytometry. *Biochemistry* **41**, 1742–1751 (2002).

29. D. J.-F. Chinnapen, *et al.*, Lipid-sorting by ceramide structure from plasma membrane to ER for the cholera toxin receptor ganglioside GM1. *Dev. Cell* **23**, 573–586 (2012).

30. P. A. Orlandi, P. H. Fishman, Filipin-dependent inhibition of cholera toxin: evidence for toxin internalization and activation through caveolae-like domains. *J. Cell Biol.* **141**, 905–915 (1998).

31. C. A. Day, A. K. Kenworthy, Functions of cholera toxin B-subunit as a raft cross-linker. *Essays Biochem.* **57**, 135–145 (2015).

32. E. B. Watkins, *et al.*, Shiga toxin induces lipid compression: a mechanism for generating membrane curvature. *Nano Lett.* (2019) https:/doi.org/10.1021/acs.nanolett.9b03001.

33. L. Johannes, Shiga Toxin-A Model for Glycolipid-Dependent and Lectin-Driven Endocytosis. *Toxins* **9** (2017).

34. R. Dasgupta, M. S. Miettinen, N. Fricke, R. Lipowsky, R. Dimova, The glycolipid GM1 reshapes asymmetric biomembranes and giant vesicles by curvature generation. *Proc. Natl. Acad. Sci. U. S. A.* **115**, 5756–5761 (2018).

35. J. C. Stachowiak, *et al.*, Membrane bending by protein-protein crowding. *Nat. Cell Biol.* **14**, 944–949 (2012).

36. I. Basu, C. Mukhopadhyay, Insights into Binding of Cholera Toxin to GM1 Containing Membrane. *Langmuir* **30**, 15244–15252 (2014).

37. M. Štefl, *et al.*, Dynamics and Size of Cross-Linking-Induced Lipid Nanodomains in Model Membranes. *Biophys. J.* **102**, 2104–2113 (2012).

38. M. Kang, C. A. Day, A. K. Kenworthy, E. DiBenedetto, Simplified equation to extract diffusion coefficients from confocal FRAP data. *Traffic Cph. Den.* **13**, 1589–1600 (2012).

39. A. K. Kenworthy, *et al.*, Dynamics of putative raft-associated proteins at the cell surface. *J. Cell Biol.* **165**, 735–746 (2004).

40. K. Bacia, D. Scherfeld, N. Kahya, P. Schwille, Fluorescence correlation spectroscopy relates rafts in model and native membranes. *Biophys J* **87**, 1034–1043 (2004).

41. P. D. J. Moens, M. A. Digman, E. Gratton, Modes of diffusion of cholera toxin bound to GM1 on live cell membrane by image mean square displacement analysis. *Biophys. J.* **108**, 1448–1458 (2015).

42. K. M. Spillane, *et al.*, High-Speed Single-Particle Tracking of GM1 in Model Membranes Reveals Anomalous Diffusion due to Interleaflet Coupling and Molecular Pinning. *Nano Lett.* **14**, 5390–5397 (2014).

43. C.-L. Hsieh, S. Spindler, J. Ehrig, V. Sandoghdar, Tracking Single Particles on Supported Lipid Membranes: Multimobility Diffusion and Nanoscopic Confinement. *J. Phys. Chem. B* **118**, 1545–1554 (2014).

44. Y. Gambin, *et al.*, Lateral mobility of proteins in liquid membranes revisited. *Proc. Natl. Acad. Sci. U. S. A.* **103**, 2098–2102 (2006).

45. J. D. Knight, M. G. Lerner, J. G. Marcano-Velázquez, R. W. Pastor, J. J. Falke, Single molecule diffusion of membrane-bound proteins: window into lipid contacts and bilayer dynamics. *Biophys. J.* **99**, 2879–2887 (2010).

46. B. P. Ziemba, J. J. Falke, Lateral diffusion of peripheral membrane proteins on supported lipid bilayers is controlled by the additive frictional drags of (1) bound lipids and (2) protein domains penetrating into the bilayer hydrocarbon core. *Chem. Phys. Lipids* **172–173**, 67–77 (2013).

47. A. Sridhar, A. Kumar, A. K. Dasmahapatra, Multi-scale molecular dynamics study of cholera pentamer binding to a GM1-phospholipid membrane. *J. Mol. Graph. Model.* **68**, 236–251 (2016).

48. S. Rissanen, *et al.*, Phase Partitioning of GM1 and Its Bodipy-Labeled Analog Determine Their Different Binding to Cholera Toxin. *Front. Physiol.* **8**, 252 (2017).

49. R. H. Massol, J. E. Larsen, Y. Fujinaga, W. I. Lencer, T. Kirchhausen, Cholera toxin toxicity does not require functional Arf6- and dynamin-dependent endocytic pathways. *Mol. Biol. Cell* **15**, 3631–3641 (2004).

50. C. A. Day, *et al.*, Microtubule motors power plasma membrane tubulation in clathrin-independent endocytosis. *Traffic Cph. Den.* **16**, 572–590 (2015).

51. H.-F. Renard, *et al.*, Endophilin-A2 functions in membrane scission in clathrin-independent endocytosis. *Nature* **517**, 493–496 (2015).

52. E. Boucrot, *et al.*, Endophilin marks and controls a clathrin-independent endocytic pathway. *Nature* **517**, 460–465 (2015).

53. A. A. Wolf, *et al.*, Attenuated Endocytosis and Toxicity of a Mutant Cholera Toxin with Decreased Ability To Cluster Ganglioside GM1 Molecules. *Infect. Immun.* **76**, 1476–1484 (2008).

54. A. T. Hammond, *et al.*, Crosslinking a lipid raft component triggers liquid ordered-liquid disordered phase separation in model plasma membranes. *Proc. Natl. Acad. Sci. U. S. A.* **102**, 6320–6325 (2005).

55. D. Lingwood, J. Ries, P. Schwille, K. Simons, Plasma membranes are poised for activation of raft phase coalescence at physiological temperature. *Proc. Natl. Acad. Sci. U. S. A.* **105**, 10005–10010 (2008).

56. L. Johannes, S. Mayor, Induced domain formation in endocytic invagination, lipid sorting, and scission. *Cell* **142**, 507–510 (2010).

57. C. Yuan, J. Furlong, P. Burgos, L. J. Johnston, The size of lipid rafts: an atomic force microscopy study of ganglioside GM1 domains in sphingomyelin/DOPC/cholesterol membranes. *Biophys. J.* **82**, 2526–2535 (2002).

58. H. Sun, L. Chen, L. Gao, W. Fang, Nanodomain Formation of Ganglioside GM1 in Lipid Membrane: Effects of Cholera Toxin-Mediated Cross-Linking. *Langmuir* **31**, 9105–9114 (2015).

59. K. Raghunathan, *et al.*, Glycolipid Crosslinking Is Required for Cholera Toxin to Partition Into and Stabilize Ordered Domains. *Biophys. J.* **111**, 2547–2550 (2016).

60. S. A. Johnson, *et al.*, Temperature-dependent phase behavior and protein partitioning in giant plasma membrane vesicles. *Biochim. Biophys. Acta* **1798**, 1427–1435 (2010).

61. M. Panasiewicz, H. Domek, G. Hoser, M. Kawalec, T. Pacuszka, Structure of the ceramide moiety of GM1 ganglioside determines its occurrence in different detergent-resistant membrane domains in HL-60 cells. *Biochemistry* **42**, 6608–6619 (2003).

62. S. Veatch, “Electro-Formation and Fluorescence Microscopy of Giant Vesicles With Coexisting Liquid Phases” in *Lipid Rafts*, Methods in Molecular Biology., T. McIntosh, Ed. (Humana Press, 2007), pp. 59–72.

63. M. Ovesný, P. Křížek, J. Borkovec, Z. Svindrych, G. M. Hagen, ThunderSTORM: a comprehensive ImageJ plug-in for PALM and STORM data analysis and super-resolution imaging. *Bioinforma. Oxf. Engl.* **30**, 2389–2390 (2014).

64. K. Jaqaman, *et al.*, Robust single-particle tracking in live-cell time-lapse sequences. *Nat. Methods* **5**, 695–702 (2008).

65. A. J. Berglund, Statistics of camera-based single-particle tracking. *Phys. Rev. E Stat. Nonlin. Soft Matter Phys.* **82**, 011917 (2010).

66. S. L. Veatch, *et al.*, Correlation Functions Quantify Super-Resolution Images and Estimate Apparent Clustering Due to Over-Counting. *PLOS ONE* **7**, 1–13 (2012).

67. W. Humphrey, A. Dalke, K. Schulten, VMD: Visual molecular dynamics. *J. Mol. Graph.* **14**, 33–38 (1996).

68. E. A. Merritt, *et al.*, Structural studies of receptor binding by cholera toxin mutants. *Protein Sci. Publ. Protein Soc.* **6**, 1516–1528 (1997).

## FIGURES

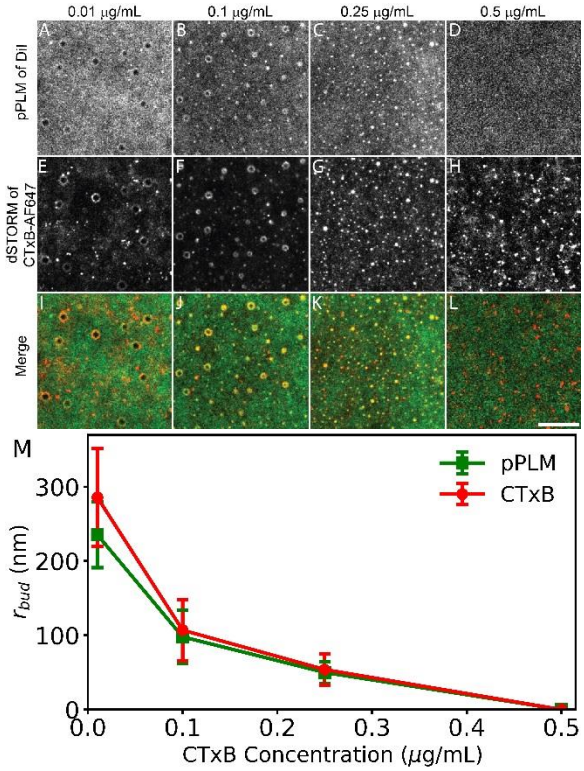


**Figure 1:** The ratio of GM1 to CTxB was controlled by varying the CTxB concentration in solution. (A-D) pPLM results show the larger membrane curvature with lower CTxB concentrations and (E-H) dSTORM images show CTxB clustering that (I-L) are co-localized in the merged images of the DiI (*green*) and CTxB (*red*). The CTxB concentrations were (A, E, I) 0.01, (B, F, J) 0.1, (C, G, K) 0.25, or (D, H, L) 0.5 μg/mL above POPC, GM1, and DiI membranes at molar ratios of 99.4 : 0.3 : 0.3. (M) Membrane bud sizes were measured from the super-resolution images to quantify the decreasing bud size with increasing the CTxB concentration. Error bars represent the standard deviation of individual bud sizes. The scale bar represents 2 μm for all panels.

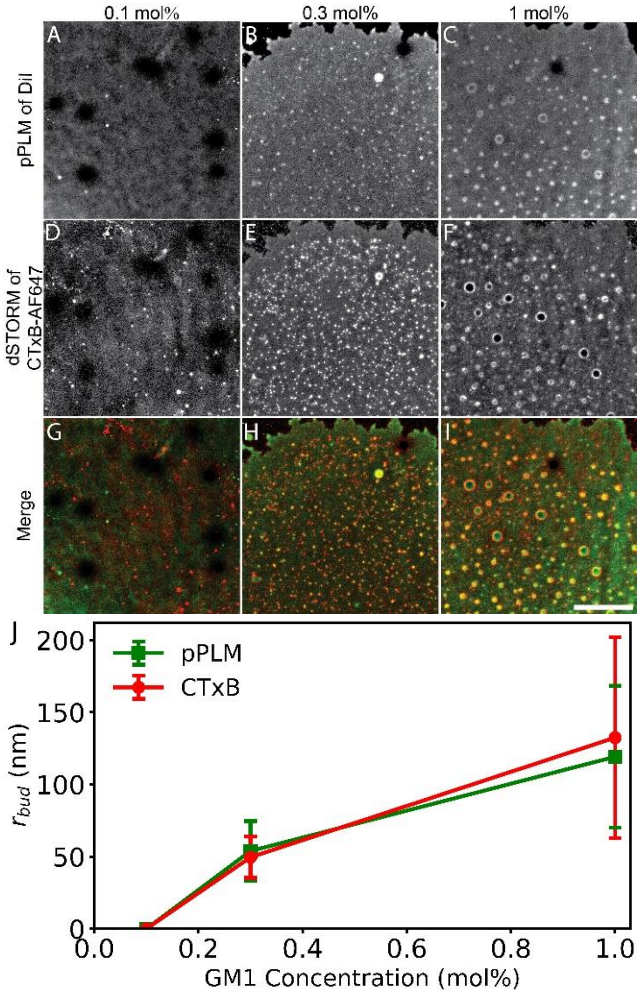


**Figure 2:** The ratio of GM1 to CTxB was controlled by varying the GM1 concentration in the membrane. (A-C) pPLM results show the larger membrane curvature features with higher the GM1 concentration and (D-F) dSTORM images show CTxB clustering that (G-I) are co-localized in the merged images of the DiI (*green*) and CTxB (*red*). GM1 was incorporated at (A, D, G) 0.1, (B, E, H) 0.3, or (C, F, I) 1 mol% with 0.3 mol% DiI and otherwise POPC membranes exposed to 0.25 μg/mL of CTxB-AF647. (J) Membrane bud sizes were measured from the super-resolution images to quantify the increasing bud size with increasing GM1 concentrations. Error bars represent the standard deviation of individual bud sizes. The scale bar represents 2 μm for all panels.

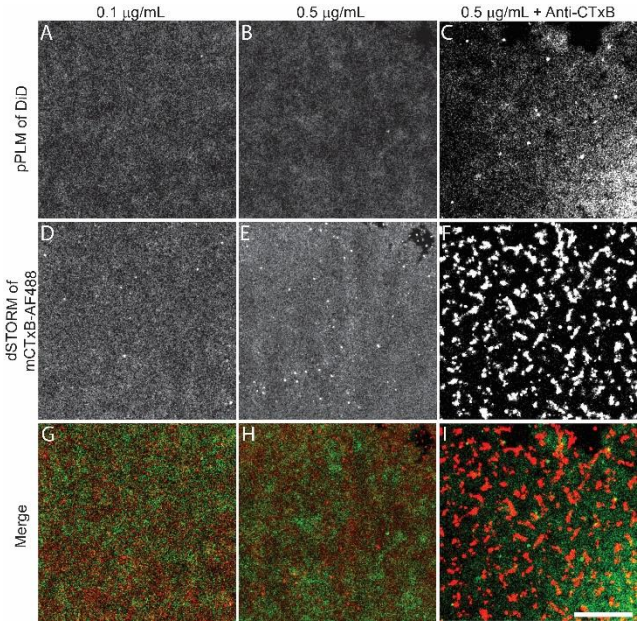


**Figure 3:** No membrane curvature was observed upon the addition of mCTxB. (A-C) pPLM results show no curvature consistent with (D, E) dSTORM images showing uniform mCTxB distributions. (G) Anti-CTxB at 100:1 dilution shows significant mCTxB clustering, but no membrane bending. (G-I) Merged images of the DiI (*green*) and CTxB-AF647 (*red*) show no coincident puncta. With a GM1 concentration of 0.3 mol%, the mCTxB concentrations of 0.1 or 0.5 μg/mL were used to mimic the protein or binding site concentration of conditions in which wtCTxB created significant membrane bending. The scale bar represents 2 μm for all panels.

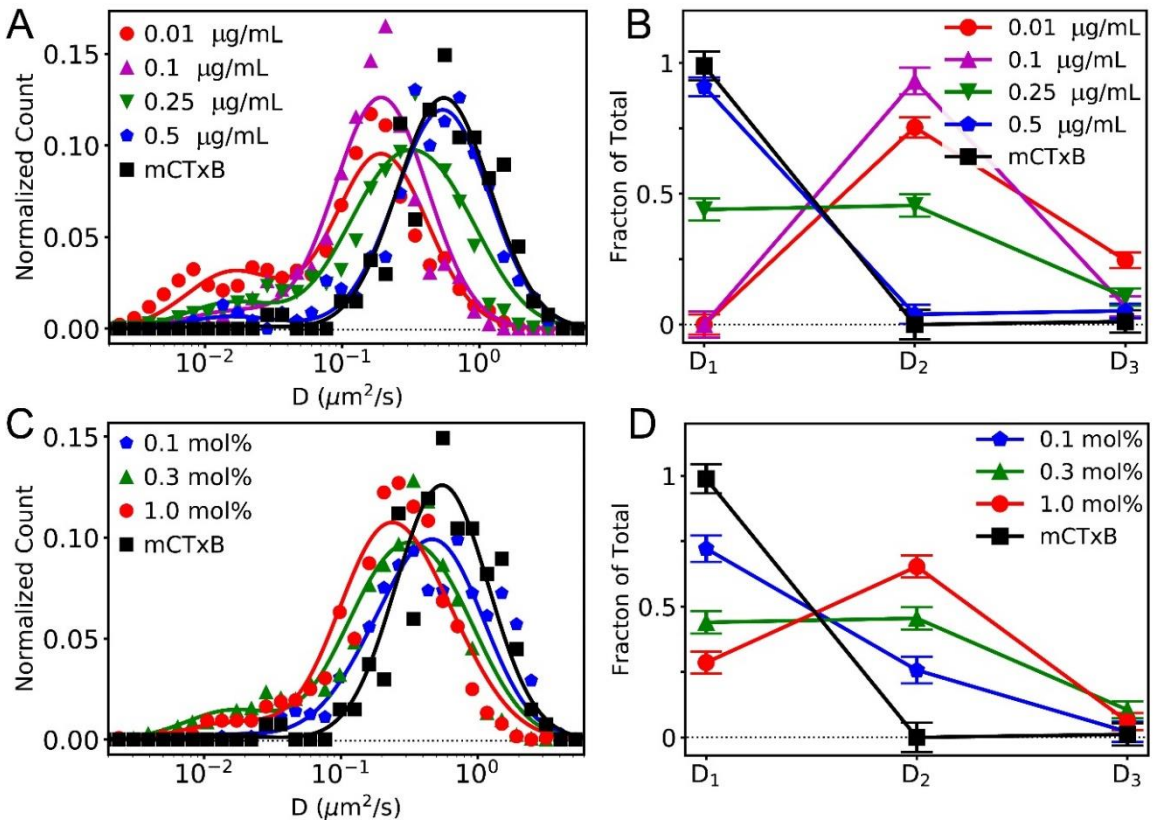


**Figure 4:** Single-particle tracking of CTxB revealed a distribution of diffusion rates for individual, membrane-bound proteins with (A, B) 0.3 mol% GM1 and varying the CTxB concentration or (C, D) 0.25 μg/mL CTxB and varying GM1 concentration. When the GM1:CTxB ratio increased, the CTxB diffusion rate decreased. The diffusion of mCTxB demonstrates the expected diffusion rate with one GM1 per CTxB. The eight different distributions fit to extract the fraction of CTxB in each experiment with 1, 2, or 3 GM1 per CTxB (Eq. 3). Fits of individual subpopulations are shown in Fig. S5.

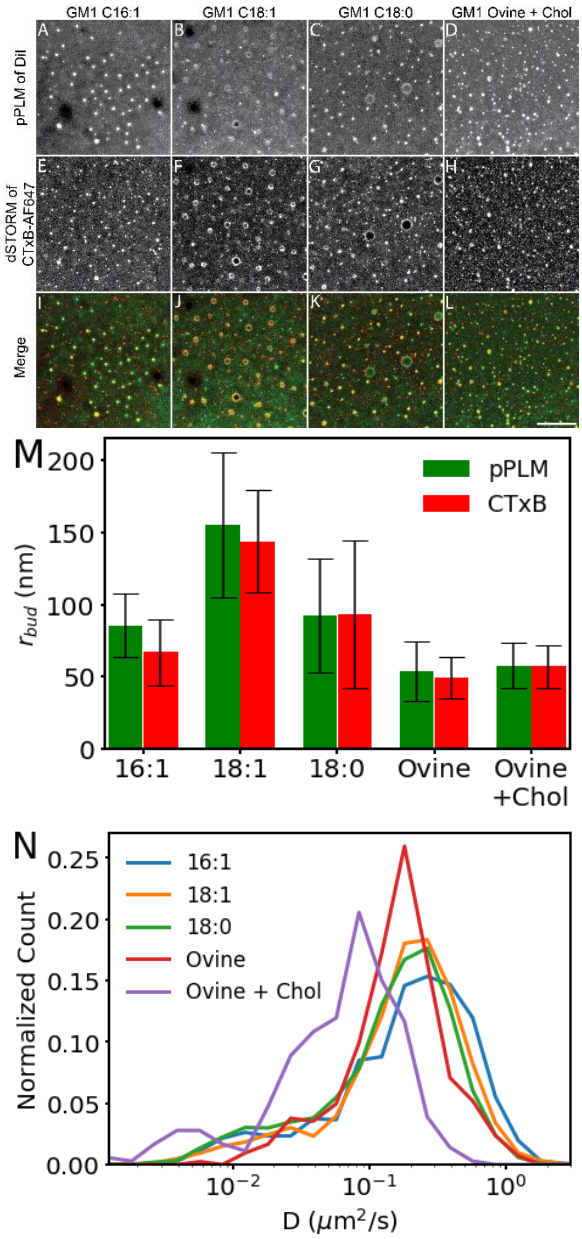


**Figure 5:** Neither altering the acyl tails of GM1 nor including cholesterol showed a correlation between lipid order and membrane curvature induction by CTxB. However, increasing the GM1 acyl tail order did correlate with decreasing CTxB diffusion rates. (A-D) pPLM images show the membrane curvature, (E-H) dSTORM images show CTxB clustering, and (I-L) merged images of the DiI (*green*) and CTxB (*red*) show their co-localization. Acyl tails of the GM1 were (A, E, I) 16:1, (B, F, J) 18:1, (C, G, K) 18:0, or commercially extracted from ovine. (D, H, L) Cholesterol addition similarly did not affect curvature induction. The scale bar represents 2 μm for (A-L). (M) Curvature was quantified by measuring the mean and standard deviation of membrane bud sizes from three repeats. The bud sizes for $GM1_{18:1}$ was significantly larger than that of $GM1_{Ovine}$ with and without cholesterol ($p$<0.05), but no other statistical differences were present. (N) The distributions of $D$ from single-molecule trajectories of CTxB demonstrate decreasing $D$ with increasing lipid order.

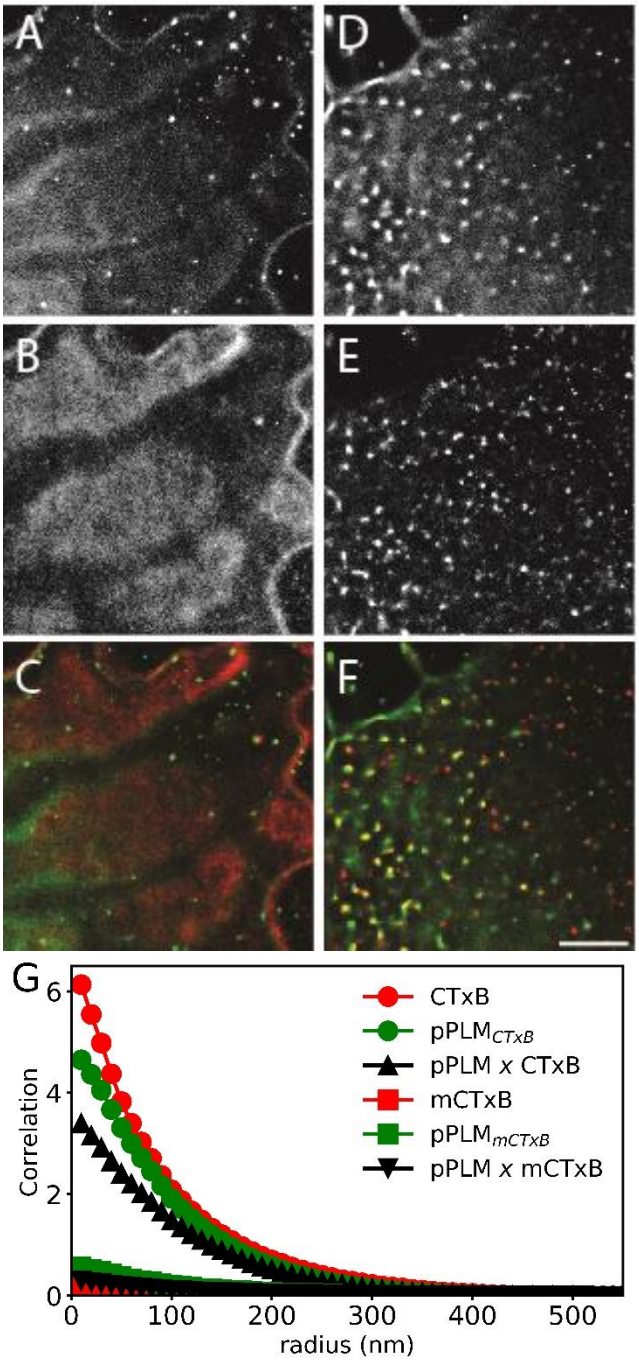


**Figure 6:** CTxB and mCTxB behaved similarly on living cells as they did on model membranes. The (A) pPLM, (B) dSTORM, and (C) merged images with mCTxB show less membrane curvature and negligible sorting of the mCTxB to the membrane curvature. The (D) pPLM, (E) dSTORM, and (F) merged images with CTxB show an increase in nanoscale membrane bending that is spatially correlated to the CTxB clustering. (G) The magnitude of the clustering of the protein and the presence of nanoscale membrane budding are quantified by the autocorrelations. The magnitude of the sorting of the CTxB and mCTxB to the membrane bending are quantified by the cross-correlations. The scale bar represents 2 μm for (A-F).

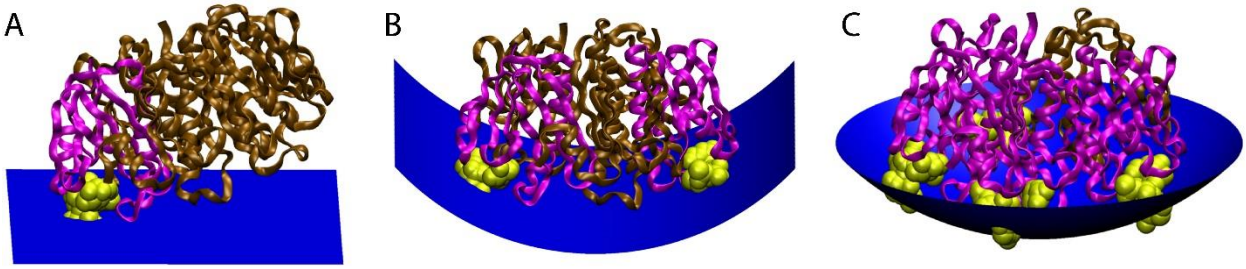


**Figure 7:** Schematics of CTxB binding to surfaces of varying curvature depending on the GM1:CTxB ratio. Of the five identical subunits of CTxB, those bound to a GM1 are colored pink, and unbound subunits are shown in brown. The terminal galactose and sialic acid of GM1 are colored yellow**.** (A) When one GM1 is bound per CTxB, there is no membrane curvature. (B) When two GM1 are bound per CTxB, a single dimension of negative curvature is induced in the membrane, such as occurs at the neck of a membrane bud or on a membrane tube. (C) When 3 or more GM1 are bound per CTxB, negative membrane curvature is generated in two dimensions. This results in a wrapping of the membrane around the CTxB, such as within an endocytic pit. The schematics were created in VMD (67) by building upon a crystal structure of CTxB (68)**.**

## SUPPLEMENTAL FIGURES

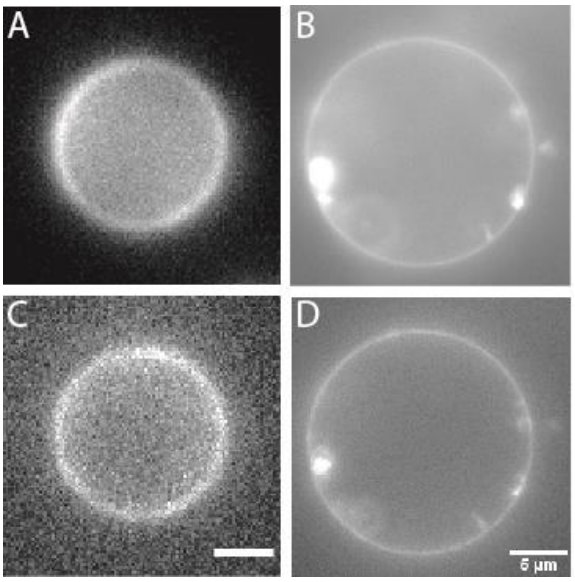


**Figure S1:** (A, C) Curvature was not created in GUVs exposed to 0.1 µg/mL mCTxB, but (B, D) curvature was created on GUVs with 0.1 µg/mL CTxB, as revealed by imaging DiI (A, B) and the protein (C, D).

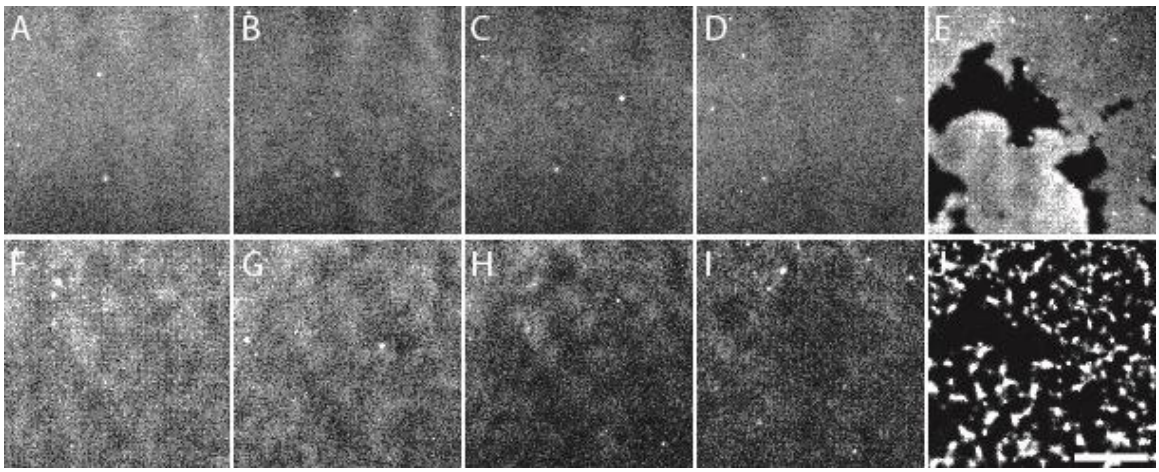


**Figure S2:** No membrane bending was observed upon the addition of 0.5 µg/mL mCTxB to membranes with 0.3 mol% GM1 even when the mCTxB was crosslinked by anti-CTxB. (A-E) pPLM images show the no membrane bending and (D-F) dSTORM images show uniform mCTxB distributions with anti-CTxB dilutions of (A, F) zero, (B, G) 1:10000, (C, H) 1:1000, or (D, I) 1:500. (E, J) With anti-CTxB dilution at 1:100, clustering of the mCTxB was observed, but no membrane bending was detected, although the edge of the SLB was readily apparent (*black area*). (J) The scale bar represents 2 µm for all panels.

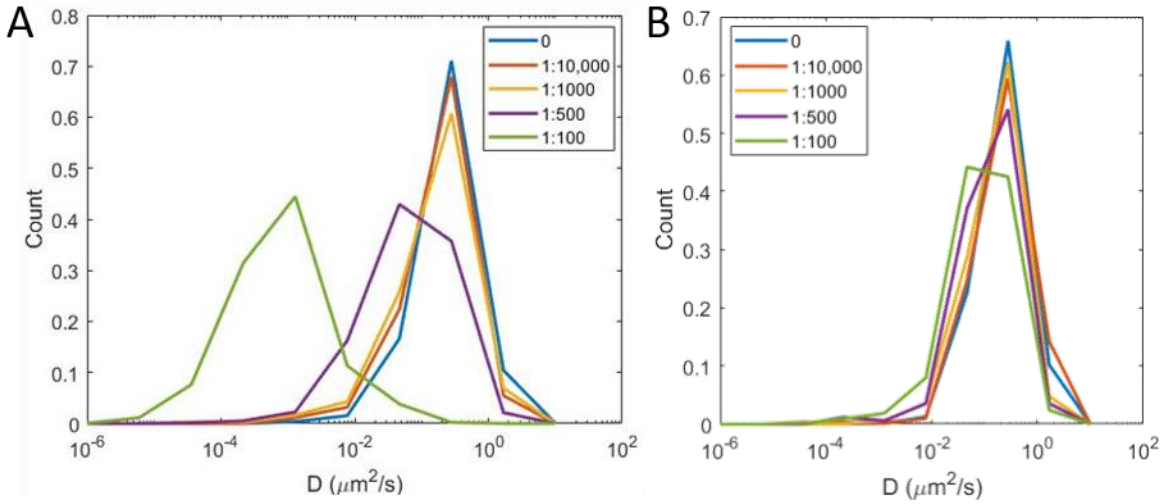


**Figure S3:** The distribution of diffusion coefficients observed for individual (A) mCTxB reveals decreased diffusion rates with increasing anti-CTxB concentrations. (B) DiI diffusion was unaffected by anti-CTxB addition.

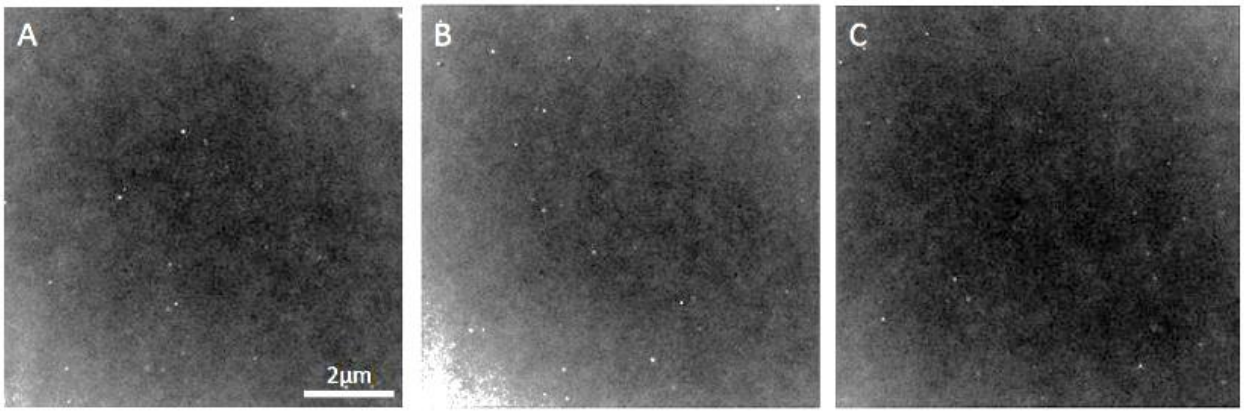


**Figure S4:** No membrane budding was observed when streptavidin was added to model membranes with POPC, DiI, and DPPE-Biotin. Super-resolution pPLM images reveal planar SLBs after 90 min of (A) 0.3, (B) 1, or (C) 3 mol% DPPE-Biotin with 0.25 µg/mL streptavidin.

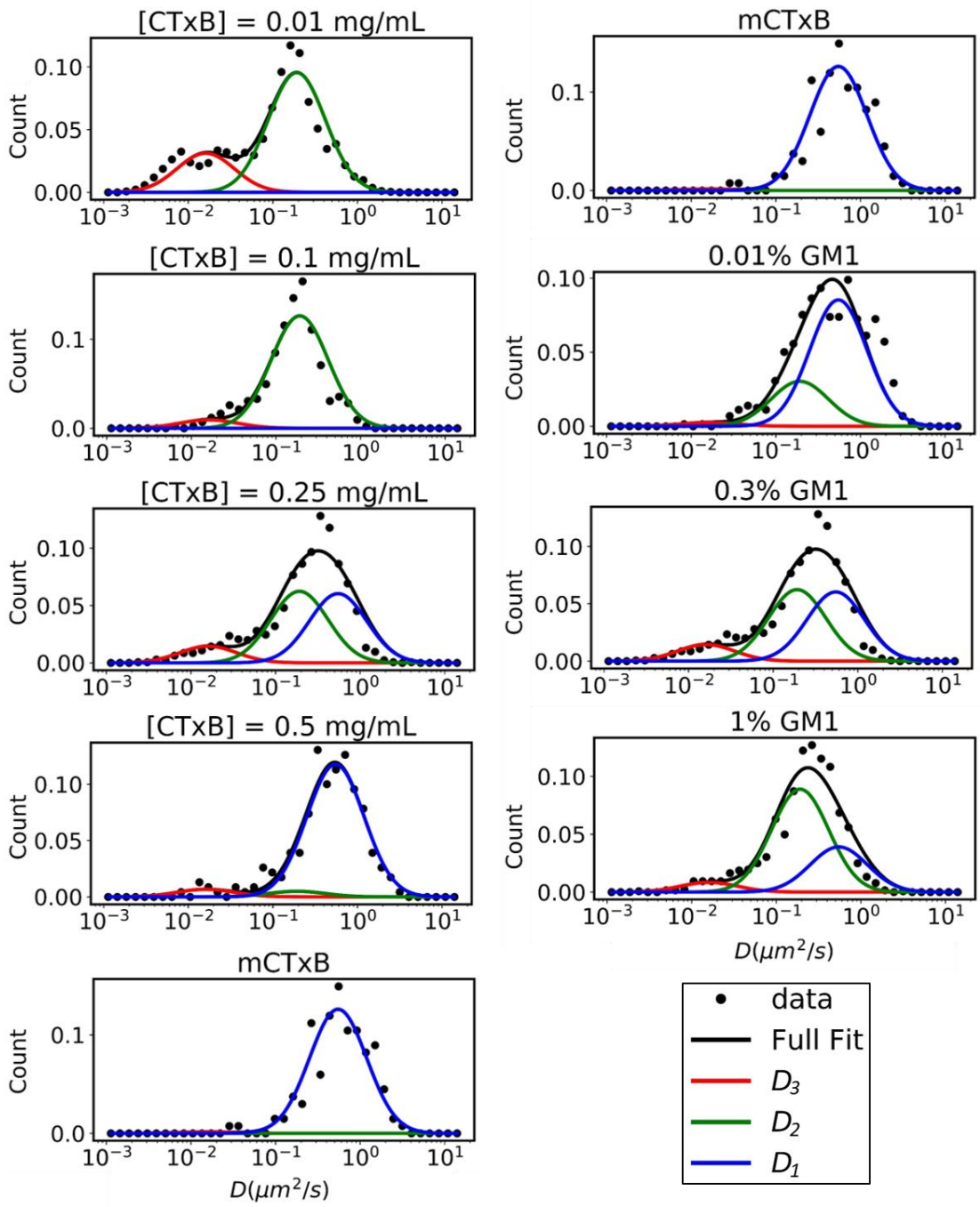


**Figure S5:** Fitting the histograms of D obtained from the experimentally varied concentrations of GM1 and CTxB revealed the subpopulations of CTxB with 1, 2, or 3 GM1 per CTxB. Each histogram of D was fit to Eq. 1 (*black line*) with the three amplitude fitting parameters unique to each experiment and the distribution corresponding to each subpopulation consistent for all experimental fits.

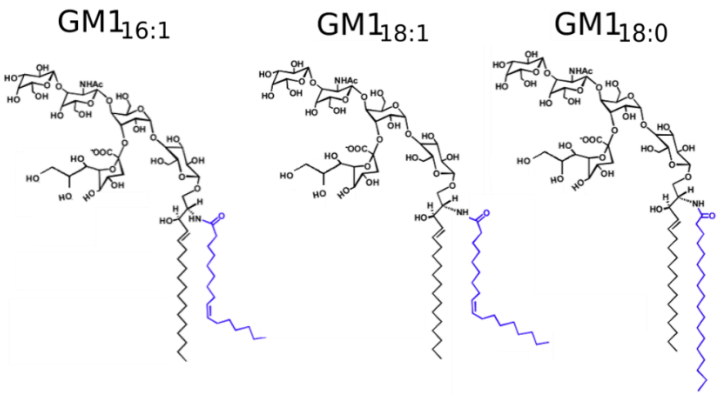


**Figure S6:** Chemical structure of custom-made GM1$_{16:1}$, GM1$_{18:1}$, and GM1$_{18:0}$. Commercially available ovine GM1 is predominantly composed of GM1$_{18:0}$.

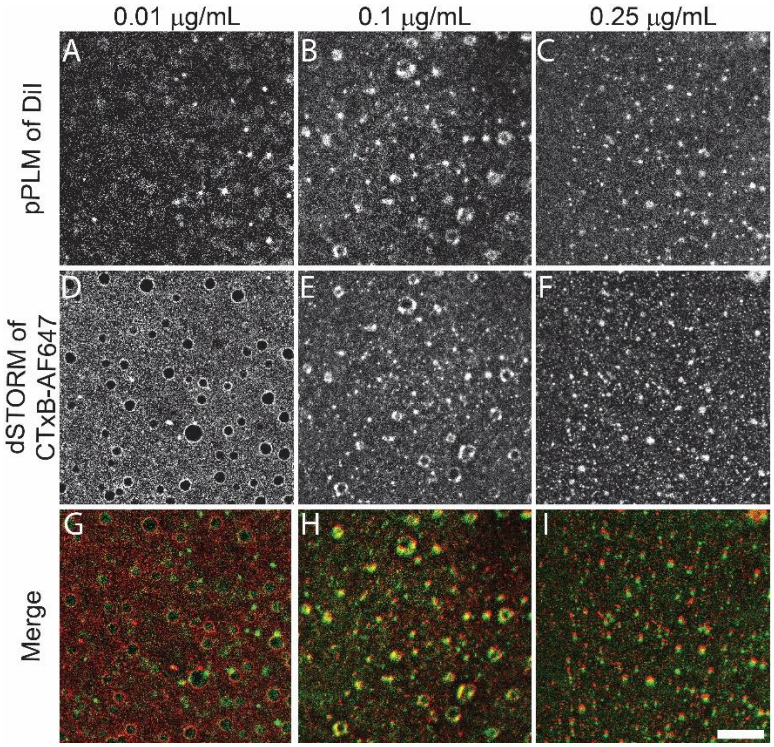


**Figure S7:** Increasing the ratio of GM1 to CTxB resulted in increasing the membrane curvature induction in model membranes of 30 mol% cholesterol. (A-C) pPLM results show the larger membrane curvature features with lower CTxB concentrations and (D-F) dSTORM images show CTxB clustering that (G-I) are co-localized in the merged images of the DiI (*green*) and CTxB (*red*). CTxB was added at (A, D, G) 0.01, (B, E, H) 0.1, or (C, F, I) 0.25 μg/mL CTxB with 0.3 mol% DiI, 0.3 mol% GM1, 30 mol% cholesterol and 69 mol% POPC membranes. The scale bar represents 2 μm for all panels.

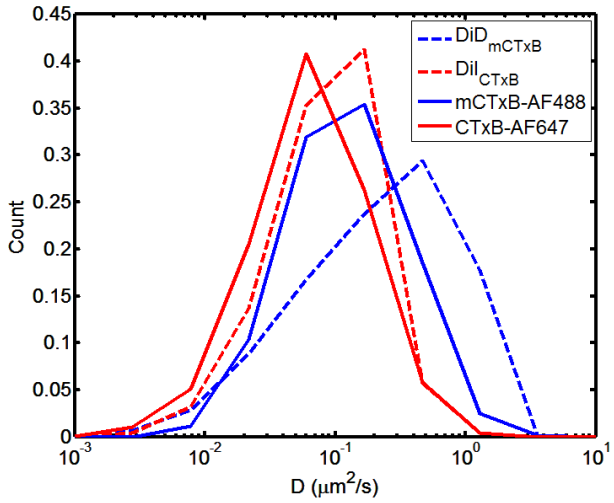


**Figure S8:** Histograms of single-molecule diffusion coefficients for DiI, DiD, CTxB, and mCTxB on living cells.